Estuarine, Coastal and Shelf Science 230 (2019) 106446

Contents lists available at ScienceDirect

Estuarine, Coastal and Shelf Science

journal homepage: http://www.elsevier.com/locate/ecss

A numerical study of residual flow induced by eddy viscosity-shear covariance in a tidally energetic estuary

Peng Cheng [a,*], Jianshan Mao [a], Fengling Yu [a], Nengwang Chen [b], Aijun Wang [c], Fanghua Xu [d]

[a] State Key Laboratory of Marine Environment Science, College of Ocean and Earth Sciences, Xiamen University, Xiamen, Fujian Province, 361102, China
[b] Fujian Provincial Key Laboratory for Coastal Ecology and Environmental Studies, College of the Environment and Ecology, Xiamen University, Xiamen, Fujian Province, 361102, China
[c] Third Institute of Oceanography, Ministry of Natural Resources, Xiamen, Fujian Province, 361005, China
[d] Ministry of Education Key Laboratory for Earth System Modeling and Department Earth System Science, Tsinghua University, Beijing, 100084, China

ARTICLE INFO

Keywords:
Estuarine circulation
Internal tidal asymmetry
Eddy viscosity–shear covariance
Numerical model

ABSTRACT

The inner regime of an estuary has unique tidal mixing processes but received relatively less attention. A numerical model was developed to investigate the tidal variability of vertical mixing and the residual flow induced by eddy viscosity–shear covariance (ESCO) in the inner regime of a tidally energetic estuary in Southeastern China. Because of migration of the saltwater/freshwater interface, the water column in the inner regime undergoes a saltwater-dominant high-water period and a freshwater-dominant low-water period during a tidal cycle. The different mixing processes of high- and low-water periods led to typical (reverse) internal tidal asymmetry, i.e. stronger (weaker) mixing during flood tides than ebb tides when the tidal range was large (small). Tidal straining was the main driver of internal tidal asymmetry during the high-water period, while the asymmetries of duration and current velocity between flood and ebb were the main drivers during the low-water period. For typical internal tidal asymmetry, the ESCO stress was negative and the ESCO flow had a two-layer structure with landward flow near the bottom and seaward flow near the surface. For reverse internal tidal asymmetry, the ESCO stress was positive and the vertical pattern of the ESCO flow was reversed. The magnitude of the ESCO flow was several times greater than that of the density-driven flow. The reverse internal tidal asymmetry occurred in the freshwater-dominant low-water period indicates that the ESCO stress could be an important driver of tidal rectification flow in homogeneous coastal waters.

1. Introduction

In the traditional theory of estuarine dynamics, the turbulent stress in the along-estuary momentum equation is parameterized as a product of an effective eddy viscosity and the vertical shear of residual velocity (Pritchard, 1956; Hansen and Rattray, 1965). The effective eddy viscosity is a constant that neglects temporal variations in vertical mixing. In tidally dominant estuaries, however, vertical mixing exhibits distinct temporal variations and is asymmetric during a tidal period, typically being stronger in flood tides than in ebb tides. The tidal asymmetry in vertical mixing has been referred to as "internal tidal asymmetry" (Jay, 1991; Jay and Musiak, 1994). A variety of processes can generate internal tidal asymmetry: tidal straining (Simpson et al., 1990; Jay, 1991) is an important driver and lateral processes also lead to estuarine stratification in either tidal phase (Lacy et al., 2003; Fram et al., 2007; Stacey et al., 2008).

As stratification increases the vertical shear of tidal current velocity, internal tidal asymmetry results in the asymmetric vertical shear of the tidal current velocity between flood and ebb tides. As a consequence, the tidally averaged velocity shows a two-layer vertical structure with seaward flow near the surface and landward flow near the bottom (Jay, 1991; Stacey et al., 2001). Because the flow structure caused by internal tidal asymmetry is similar to that of gravitational circulation (or density-driven flow), Jay (1991) proposed that the widely observed two-layer estuarine circulation is driven mainly by internal tidal asymmetry rather than by the along-estuary density gradient.

The contribution of internal tidal asymmetry to the generation of estuarine circulation indicates that the tidal variation of eddy viscosity in the friction term in the Reynolds averaged along-estuary momentum equation cannot be neglected. The turbulent stress term is, therefore,

* Corresponding author.
E-mail address: pcheng@xmu.edu.cn (P. Cheng).

https://doi.org/10.1016/j.ecss.2019.106446
Received 12 February 2019; Received in revised form 6 October 2019; Accepted 18 October 2019
Available online 22 October 2019

decomposed as

$$\overline{K_m \frac{\partial u}{\partial z}} = \overline{K_m} \frac{\partial \overline{u}}{\partial z} + \overline{K_m' \frac{\partial u'}{\partial z}}, \quad (1)$$

where $u = \overline{u} + u'$, $K_m = \overline{K_m} + K_m'$, the overbar indicates the tidal average, the prime indicates the tidal variation, K_m represents the vertical eddy viscosity, u represents the along-estuary velocity (x-direction), and z represents the vertical direction (Geyer et al., 2000). The covariance of the tidal fluctuation of eddy viscosity and the vertical shear of velocity, i.e., the last term in Eq. (1), appears in the momentum equation and acts as a driver of estuarine circulation. Of particular note is that the covariance can be generated from a variety of processes. In addition to internal tidal asymmetry (Jay, 1991), the tidal variability of vertical velocity shear is largely caused by lateral processes in wide estuaries with transverse varying bathymetry (Burchard and Schuttelaars, 2012). Therefore, Dijkstra et al. (2017) proposed the concept of eddy viscosity–shear covariance (ESCO) to generalize the physical meaning of the covariance term. They also showed that the ESCO flow could be generated by the interaction between the gravitational circulation and the temporal variation of eddy viscosity. In this study, the term of "ESCO flow" was used in place of other terms used in previous studies, such as tidal-straining-induced flow (Burchard and Hetland, 2010) and asymmetric-tidal-mixing-induced flow (Cheng et al., 2010).

As generic models can be used to focus on a specific physical process through model setup, they have been extensively used to investigate the residual flow induced by internal tidal asymmetry. Based on one-dimensional numerical models, Stacey et al. (2008) illustrated that a tidal wave with periodic stratification produces a two-layer tidal mean flow. Furthermore, Burchard and Hetland (2010) showed that ESCO flow has twice the magnitude of density-driven flow and is therefore the dominant component of residual currents in periodically stratified estuaries. Cheng et al. (2010) investigated the along-estuary pattern of ESCO flow using a two-dimensional analytical model. Their results demonstrated that internal tidal asymmetry can generate a two-layer residual circulation with a vertical structure similar to that of gravitational circulation. Also, larger asymmetries in vertical eddy viscosity produce stronger residual currents, and reverse tidal mixing asymmetry (i.e., the vertical eddy viscosity is stronger during the ebb tide than the flood tide) generates a vertical profile of residual flow opposite to that produced by typical tidal mixing asymmetry. To further examine ESCO flows in estuaries with strong stratification, Cheng et al. (2011, 2013) conducted a series of generic numerical experiments and showed that the vertical structure and relative importance of ESCO flow are related to stratification. Burchard et al. (2011) examined the transverse structure of ESCO flow in irrotational estuarine channels and found that when the Simpson number, which measures the competition between tidal straining and tidal stirring to determine stratification in an estuary (Simpson et al., 1990; Stacey et al., 2001), is low, the ESCO flow supports the two-layer density-driven flow and has a clear lateral structure with the seaward flow concentrated on the top of the thalweg and the landward flows concentrated near the bed of shoals. Chen and de Swart (2018) conducted a series of numerical experiments to investigate the effects of the along-estuary bottom slope and tidal constituents on ESCO flow. They separated the ESCO flow into several components corresponding to different tidal harmonics and showed the along-estuary patterns of those components. In particular, they found that the quarter-diurnal tide is the main driver of the ESCO flow in the upper reach and near the mouth.

Those previous generic studies have revealed the essential characteristics of internal tidal asymmetry and ESCO flow. Observational studies have obtained evidence of internal tidal asymmetry and revealed the major role of tidal straining in controlling the mixing during both flood and ebb tides (i.e. Simpson et al., 2005; Becherer et al., 2011, Pu et al., 2015). However, an examination of ESCO flow in real estuaries is still missing. In particular, the inner regime of estuaries, which is near the head of the salt intrusion (Hansen and Rattray, 1965), has unique tidal mixing processes compared to the central regime because of the migration of the saltwater/freshwater interface (which can be represented using the 1 psμ isohaline surface). The aim of this study was to investigate the internal tidal asymmetry and ESCO flow in the inner regime of a tidally energetic estuary using a three-dimensional numerical model. The specific objectives are to examine the temporal variations of vertical mixing under different tidal ranges, and to understand the characteristics of the ESCO flow.

The remainder of this paper is structured as follows. In section 2, the model configuration and validation are described. In section 3, the numerical model results are used to reveal the different tidal variations in vertical eddy viscosity during spring and neap tides, and to explore the cross-estuary pattern and temporal variation of ESCO flow. In section 4, the discussion concentrates on 1) ESCO stress of barotropic tides, 2) the drivers of the vertical shear of tidal current velocity, 3) the scales of ESCO flow, and 4) the role of lateral circulation in estuarine dynamics. Section 5 summarizes the main findings of this study.

2. Numerical model

2.1. Study site

The estuary selected for this study is the Jiulong River estuary which is located on the western side of the Taiwan Strait along the southeast coast of China (Fig. 1). The bathymetry of the estuary is complex, with extensive islands and intertidal mudflats developed in the middle of the estuary (see the regions above 0-m isobars in Fig. 1). The water depth is generally less than 15 m (at the lowest low water datum). The mean tidal range is 3.9 m, and the maximum range is 6.4 m (Jiang and Wai, 2005; Wang et al., 2013). The estuary has two large tributaries, the North Stream and the West Stream. The mean annual river discharge is 1.24×10^{10} m^3, with approximately 70% of this discharge occurring during the wet season (April to September), when typhoons frequently occur (Liu et al., 1994). The river runoff mainly flows into the south channel of the estuary and enters Xiamen Bay (Guo et al., 2011). The South Brook is a smaller tributary that discharges into the middle estuary. Because of its small discharge, the South Brook was not considered in this study.

2.2. Model configuration

A three-dimensional hydrodynamic model was developed for the Jiulong River estuary based on the Regional Ocean Modeling System (ROMS) that is a free surface, hydrostatic, primitive equation ocean model that uses stretched, terrain-following vertical coordinates and orthogonal curvilinear horizontal coordinates on an Arakawa-C grid (Haidvogel et al., 2000; Shchepetkin and McWilliams, 2005). The model domain included the Jiulong River estuary, Xiamen Bay and a part of the Taiwan Strait to facilitate free changes across the estuary mouth (Fig. 2). The bathymetry was obtained by digitalizing the navigation charts of the Jiulong River estuary and its adjacent regions published by the Navigation Guarantee Department of the Chinese Navy Headquarters. An orthogonal curvilinear coordinate system was designed to follow the axis of the Jiulong River estuary, giving higher horizontal resolution in the estuary. The grid spacing was 48–800 m, and the total number of grid points was 339×165. The vertical dimension was discretized with 15 uniformly distributed sigma layers. The vertical eddy viscosity and diffusivity were computed using the k-ω turbulence closure. Horizontal eddy viscosity and diffusivity were scaled by grid size, and the coefficient for the largest grid size was set to 1.0 m^2/s.

The model was forced by tides at the offshore open boundary, by river discharge at the upstream ends of the two tributaries, and by atmospheric forcing on the water surface. Tidal forcing at the open boundary was specified using the Oregon State University (OSU) global inverse tidal model of TPXO.8.0 (Egbert et al., 1994; Egbert and

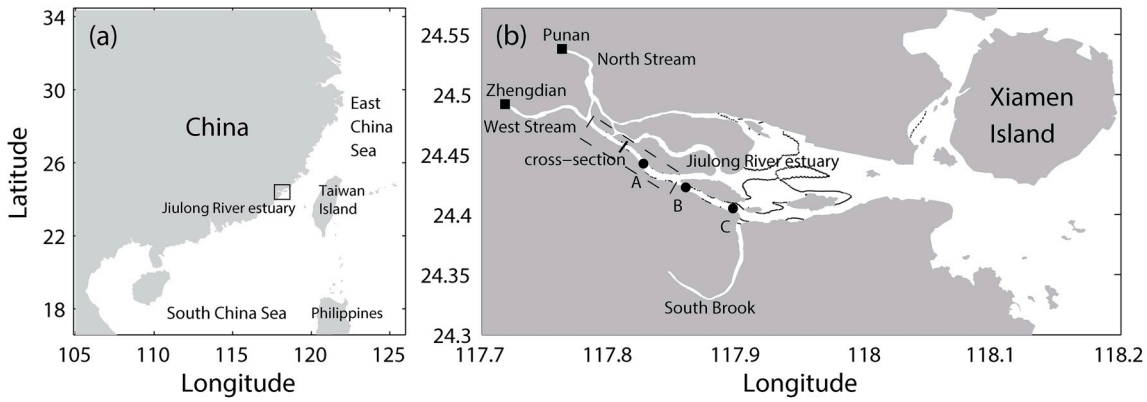

Fig. 1. Location (a) and main body (b) of the Jiulong River estuary. In (b), solid circles indicate observation stations, solid squares denote hydrological gauges, the cross-channel straight line shows the selected cross-estuary section from the numerical model, the dashed contours represent 0-m isobars and the dashed box in the upper stream of the channel shows the inner regime.

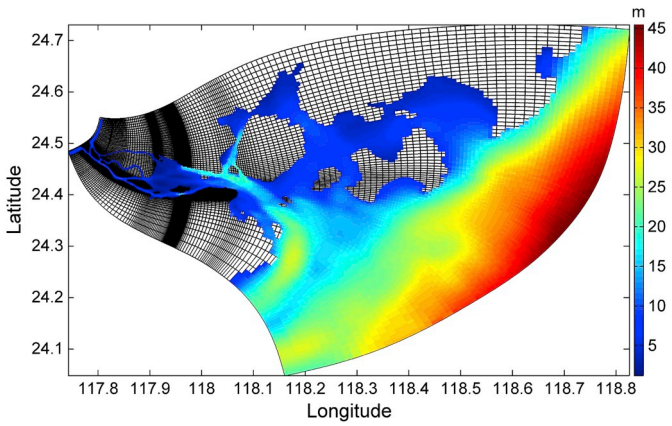

Fig. 2. Numerical model grid and bathymetry (shown in color) of the study site. The grid is subsampled by a factor of 2 for clarity.

Erofeeva, 2002). All 13 of the tidal constituents extracted from the OSU global tidal model (M_2, S_2, N_2, K_2, K_1, O_1, P_1, Q_1, M_4, MF, MM, MS_4, and MN_4) were applied. The open ocean boundary conditions for the barotropic component were the Chapman condition for surface elevation and the Flather condition for barotropic velocity. The open boundary condition for the baroclinic component was the Orlanski-type radiation condition. Ambient currents, temperature, and salinity extracted from the global model HYCOM were nudged into the open boundary with a relaxation timescale of 3 days for inflows. Daily river discharge and water temperature data (http://xxfb.hydroinfo.gov.cn/) were available for two hydrological stations (Punan at the North Stream and Zhengdian at the West Stream, see Fig. 1b). Because the two gauges are located behind two dams, the boundary condition on the heads of the two streams was defined as a wall with freshwater point sources through which river discharge was imposed as a mass transport. The atmospheric forcing was extracted from the NCEP climate forecast system reanalysis (CFSR) database (Saha and Coauthors, 2014), and the surface wind stress and net heat fluxes were computed using the bulk parameterization. Simulations were performed from 1 January 2014 to 31 December 2015, and the results of the second year (2015) were used for the analysis.

2.3. Model validation

The Jiulong River estuary has several channels separated by islands and shoals. The channel along the south coast (i.e. the south channel) is the main navigation channel of the estuary and is the locus of this study. The other channels are shallow and accessible only by small boats. Three stations (i.e. A, B, and C; see Fig. 1b) were selected to represent the upper, center, and lower regions of the inner regime, and three moorings were deployed at the three stations during 6–8 May 2015. During the observation period, the river discharge was 550 m^3/s, and the tidal range was about 2 m, a typical tide in the estuary. A 1200-kHz Acoustic Doppler Current Profiler (ADCP) was mounted on the bottom of each mooring looking upward, and a boat was anchored nearby. Forty vertical profiles of temperature and salinity were measured hourly from the boat using a Sea & Sun Technology CTD 48M probe. In each CTD profile, turbidity was also recorded and was converted to suspended sediment concentration using water samples. The maximum suspended sediment concentration during the observation was about 0.7 kg/m^3 at station C, which produces a density anomaly of 0.44 kg that was equivalent to the effect of a change in salinity of 0.57 psμ. Because the change in salinity is about 10 psμ at station B and is about 15 psμ at station C, the influence of suspended sediment on water density was not taken into account in evaluating water column stratification.

In order to quantitatively compare the model results and observations, Warner et al. (2005) introduced a measure of model skill:

$$Skill = 1 - \frac{\sum |X_{mod} - X_{obs}|^2}{\sum \left(|X_{mod} - \overline{X}_{obc}| + |X_{obs} - \overline{X}_{obc}|\right)^2}, \quad (2)$$

where X is the variable being compared with a time mean $\overline{\overline{X}}$ and the subscripts "mod" and "obs" stand for model results and observations. This parameter describes the degree to which the observed deviations about the observed mean correspond to the predicted derivations about the observed mean. Perfect agreement between model results and observations would yield a skill of one, while complete disagreement yields a skill of zero.

The salinity and velocity profiles for the observed and modeled results are shown in Fig. 3. Saltwater appeared during the high-water period, and freshwater dominated the lower-water period, generating periodic stratification over a tidal cycle. Although the model slightly overestimated the salinities at station A and slightly underestimated those at stations B and C during the high-water period, it generally predicted reliable tidal variations of salinity in the inner regime. Due to a malfunction of the ADCP, velocity data were not collected at station A. The velocities at stations B and C were rotated in along- and cross-estuary directions using the principal component analysis method. The model captured the general tidal variability of the along-estuary velocity component: the tidal current velocity was less sheared during the flood tide and was highly sheared during the ebb tide, consistent with the changes in stratification. The skills of the salinities were larger than 0.94 with the exception of station A, and the skills of the velocities were greater than 0.82 (Table 1), showing good performance of the numerical

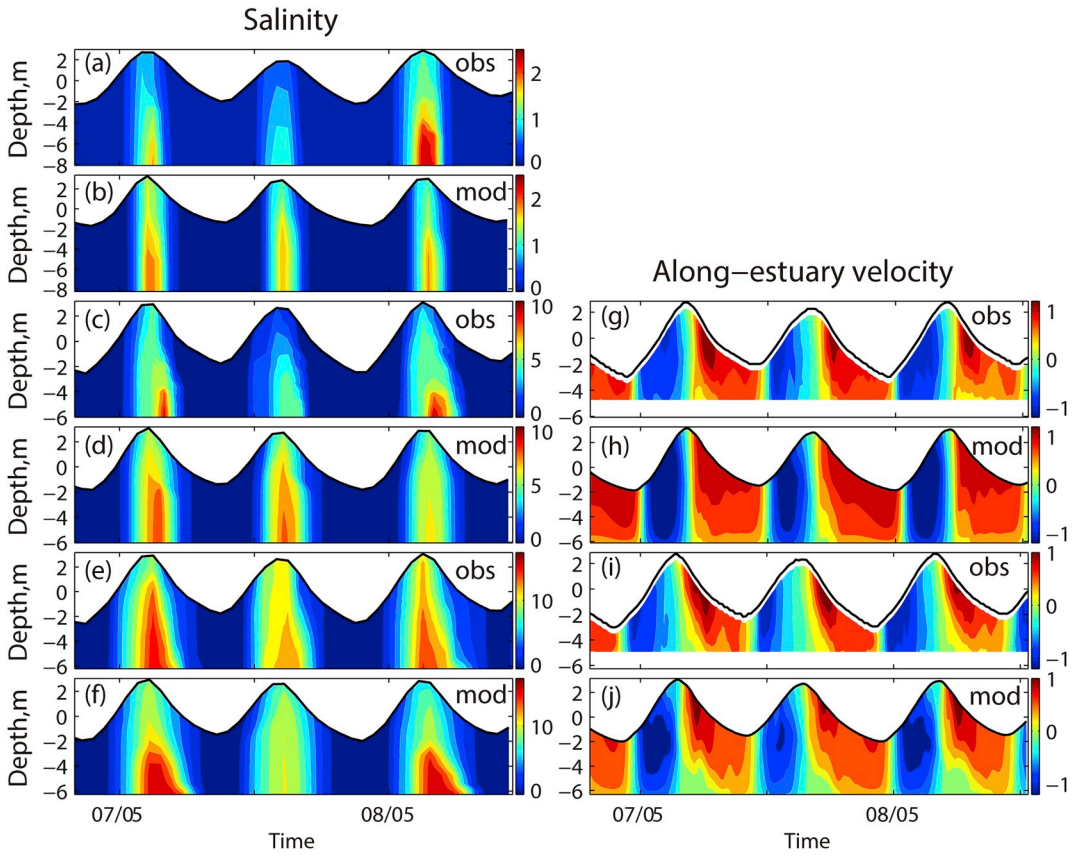

Fig. 3. Comparison of the observed and modeled salinities (left column) and along-estuary velocities (right column) at the observation stations. The observations are shown in (a), (c), (e), (g) and (i) with the label "obs" and the model results are shown in (b), (d), (f), (h) and (j) with the label "mod". The first two rows show station A, the middle two rows show station B, and the bottom two rows show station C.

model. The skill increased from station A toward station C, indicating that the model performed better in the seaward part of the inner regime.

3. Results

3.1. Tidal variation of vertical eddy viscosity

The tidal variation in vertical mixing along the south channel was examined using the transverse-section-averaged vertical eddy viscosity. Two tidal cycles from the one-year model results were selected to show the distribution of internal tidal asymmetry along the south channel (Fig. 4). The river discharge was approximately steady (about 250 m^3/s) during the two selected tidal cycles, so that the changes in tidal mixing were mainly determined by tidal amplitude. When the tidal range was relatively large (e.g. during the spring tide), the entire south channel exhibited typical internal tidal asymmetry, i.e. the eddy viscosity was larger during flood than ebb tides (Fig. 4a). When the tidal range was small (e.g. during the neap tide), the inner regime (from 0 to 8 km; also see the dashed box in Fig. 1b) exhibited reversed internal tidal asymmetry, i.e. the eddy viscosity was larger during ebb than flood tides, while the rest of the channel still exhibited typical internal tidal asymmetry (Fig. 4b). Based on the tidally averaged section-mean salinity (Fig. 4c), the salinity in the inner regime ranges nearly from 0 to 3 psμ.

Table 1
Model skills of the model and observation comparison.

Station	Salinity	Along-estuary velocity
A	0.81	
B	0.94	0.82
C	0.95	0.87

To further illustrate the two types of internal tidal asymmetry exhibited during the spring and neap tides, a comparison of the vertical profiles of along-estuary velocity, salinity, and vertical eddy viscosity in the thalweg of a selected cross-section located in the middle of the inner regime (4 km from the head of the channel, Fig. 1b) during the two selected tidal cycles is presented in Fig. 5. The tidal wave in the Jiulong River estuary has the characteristics of a standing wave. The slack water occurred at the high water period (Fig. 5a, d). A notable feature of the tidal wave is the longer ebb tide that has weaker currents during the spring tide and stronger currents during the neap tide. Two processes contributed to generate this tidal velocity asymmetry: 1) the Jiulong River estuary has extensive inter-tidal flats that store water during the flood tide and release water to the channel during the ebb tide, resulting in a shorter flood and a longer ebb in the channel, as elaborated in Friedrichs and Aubrey (1988); and 2) the river discharge produces a barotropic flow with a magnitude comparable to that of the tidal current such that the ebb has a longer duration and stronger currents (Fig. 5d shows that the magnitude of the tidal current velocity during the neap tide is about 0.5 m/s, and Fig. 7a shows that the runoff-induced flow has a magnitude of 15 cm/s). The tidal current velocity was less sheared during the later flood and was highly sheared during the early ebb. This asymmetric shear of the tidal current velocity was more apparent during the spring tide than during the neap tide.

It is apparent from the salinity profiles that the periodically stratified water column was related to the migration of the freshwater/saltwater interface in the inner regime. Saltwater appeared only for a couple of hours of high water (i.e., from late flood to early ebb tides), whereas freshwater dominated the low-water period. The high-water period was periodically stratified in the spring tide and was permanently stratified in the neap tide due to the weak tidal currents (Fig. 5b, e). The intratidal

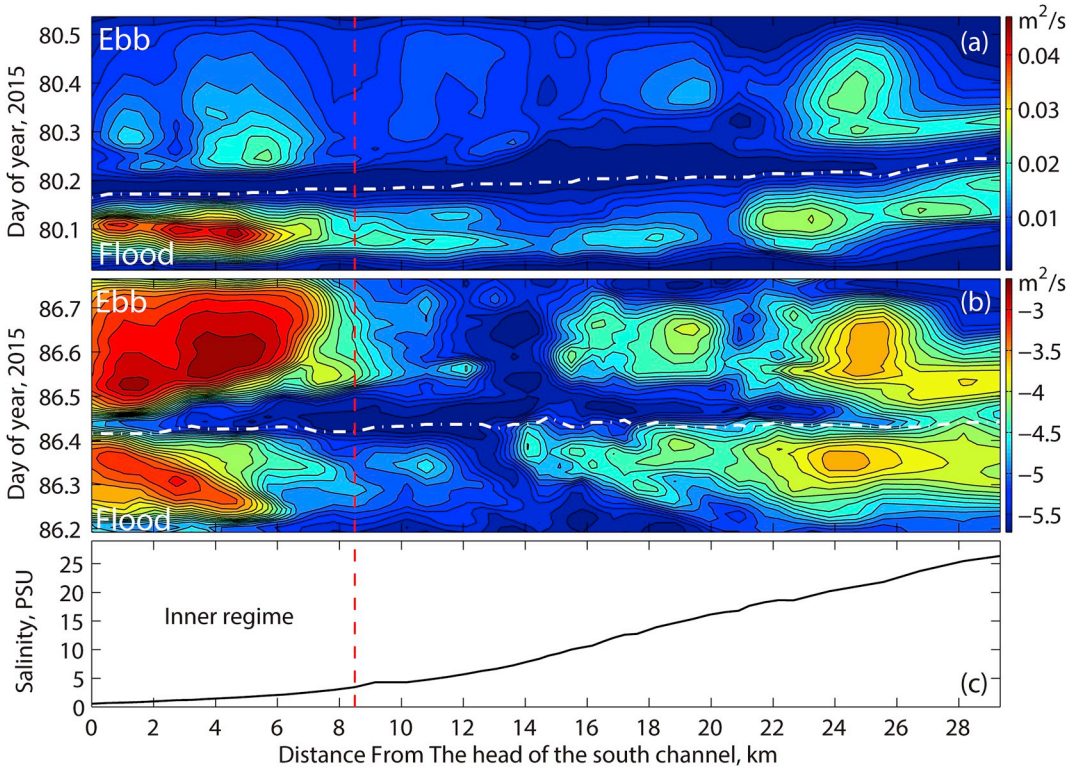

Fig. 4. Cross-section averaged vertical eddy viscosities during a tidal period in spring (a) and neap (b) tides and year-mean salinity (c) along the south channel of the Jiulong River estuary. The results are from the numerical model and the values in (b) are in the natural logarithm scale. The white lines in (a) and (b) separate flood and ebb tides, and the vertical red lines divide the estuary channel into two regimes.

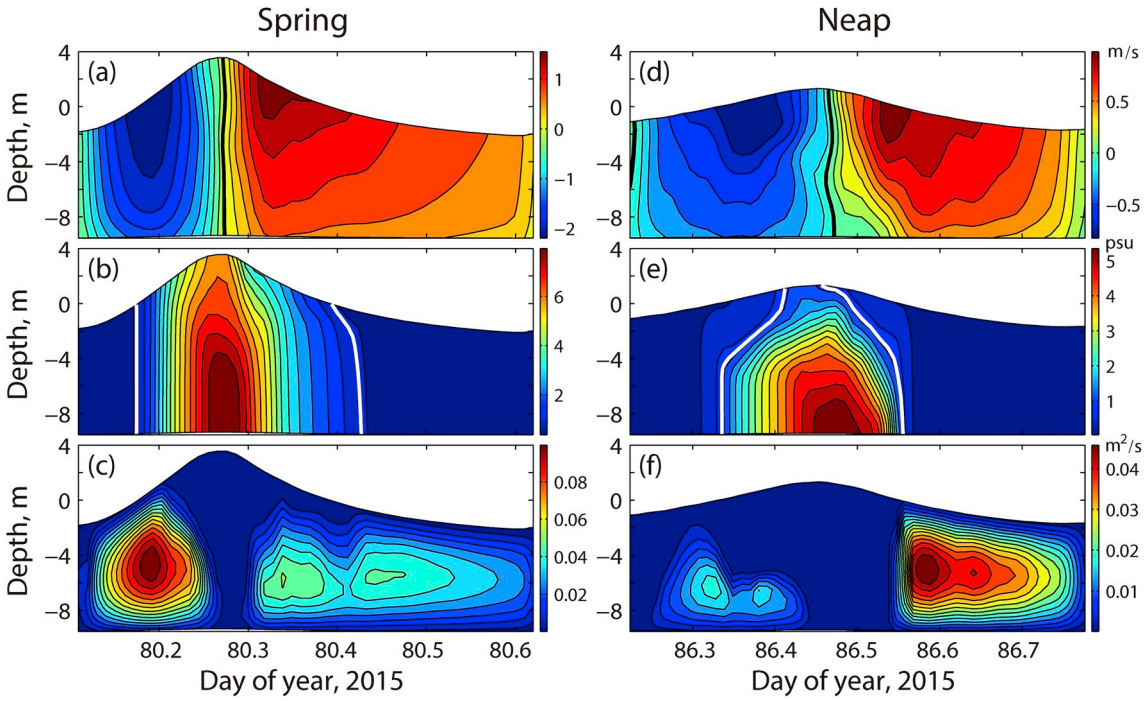

Fig. 5. Tidal variations of the along-estuary velocity (a, d), salinity (b, e), and vertical eddy viscosity (c, f) in the thalweg of the selected cross-section during spring (left column) and neap (right column) tides. The black lines in (a) represent 0 m/s, and white lines in (b) represent 1 psμ.

variation of the vertical eddy viscosity consisted of two parts corresponding to the high- and low-water periods (Fig. 5c, f). During the high-water period, mixing was related to both stratification and the strength of the tidal current. Consequently, the tidal mixing was stronger during later flood than early ebb tides, showing typical internal tidal asymmetry, with the smallest eddy viscosities appearing around the high water (slack water). During the low-water period, the mixing was a function only of tidal current velocity that produced typical internal

tidal asymmetry during the spring tide and reverse internal tidal asymmetry during the neap tide due to the tidal velocity asymmetry. The combination of tidal mixing processes in the high- and low-water periods determined the internal tidal asymmetry of the entire tidal cycle. During the spring tide, both the high- and low-water periods underwent typical internal tidal asymmetry. During the neap tide, the mixing process in the low-water period overwhelmed that during the high-water period, resulting in reverse internal tidal asymmetry.

3.2. The ESCO flow

Estuarine circulation consists of various components driven by different mechanisms. To understand the residual flow induced by ESCO mechanism, it is necessary to separate each component from estuarine circulation. Cheng (2014) developed a method to decompose three-dimensional estuarine circulation by solving coupled along- and cross-estuary momentum equations. Because the south channel of the Jiulong River estuary is very narrow (about 200 m in the inner regime), the Coriolis term in the along-estuary momentum equation is negligible compared to other forcing terms, such that the cross-estuary momentum equation can be decoupled from the along-estuary momentum equation. Hence, a simplified two-dimensional decomposition method for a narrow cross-estuary section was applied in this study. The governing equations included the along-estuary momentum and continuity equations:

$$\overline{u\frac{\partial u}{\partial x}}+\overline{v\frac{\partial u}{\partial y}}+\overline{\omega\frac{\partial u}{\partial \sigma}}-f\overline{v}=-g\frac{\partial \overline{\eta}}{\partial x}-\frac{g}{\rho_0}\left[\frac{\partial}{\partial x}\left(\overline{D\int_{\sigma}^{0}\rho d\sigma'}\right)+\overline{\rho\sigma\frac{\partial D}{\partial x}}\right]$$

$$+\overline{Z}\frac{\partial}{\partial \sigma}\left(\overline{K_m}\frac{\partial \overline{u}}{\partial \sigma}\right)+\frac{\partial ESCO}{\partial \sigma}, \tag{3a}$$

$$ESCO=\overline{Z}\overline{K'_m\frac{\partial u'}{\partial \sigma}}+\overline{Z'\frac{\partial}{\partial \sigma}\left(K'_m\frac{\partial u'}{\partial \sigma}\right)}+\overline{Z'\frac{\partial}{\partial \sigma}\left(\overline{K_m}\frac{\partial u'}{\partial \sigma}\right)}+\overline{Z'\frac{\partial}{\partial \sigma}\left(K'_m\frac{\partial \overline{u}}{\partial \sigma}\right)}, \tag{3b}$$

$$\int_0^B\int_{-1}^{0}H\overline{u}d\sigma dy+\int_0^B\int_{-1}^{0}\overline{\eta u'}d\sigma dy=R, \tag{3c}$$

where v is the velocity in cross-estuary (y) direction, ω is the vertical velocity in the sigma (σ) coordinate, f is the Coriolis parameter, g is the gravitational acceleration, ρ_0 is the reference water density, ρ is the water density, H is the mean water depth, η is the water surface elevation, $D=H+\eta$, $1/D^2=\overline{Z}+Z'$, B is the width of the estuary channel, and R is the river discharge. Sigma coordinates were used in the decomposition method to overcome the difficulty in calculating the time mean velocity around the mean water surface. The physical meaning of the residual velocity in the sigma coordinates is referred to as a semi-Lagrangian velocity (see appendix A in Cheng et al., 2013). The last three terms in Eq. (3b) result from the expansion of $1/D^2$, and the combination of the last four terms is the ESCO stress. The estuarine circulation was considered to have six components, and the solutions can be obtained by solving the equation pairs for the six components. Here, only the solution for the ESCO flow ($\overline{u_E}$) is presented:

$$\overline{u_E}=\frac{g}{\overline{Z}}\frac{\partial \overline{\eta_E}}{\partial x}\int_{-1}^{\sigma}\frac{\sigma'}{\overline{K_m}}d\sigma'-\frac{1}{\overline{Z}}\int_{-1}^{\sigma}\frac{[ESCO]}{\overline{K_m}}d\sigma'. \tag{4a}$$

$$\frac{\partial \overline{\eta_E}}{\partial x}=\frac{\int_{-1}^{0}\int_{-1}^{\sigma}\frac{[ESCO]}{\overline{K_m}}d\sigma' d\sigma}{g\int_{-1}^{0}\int_{-1}^{\sigma}\frac{\sigma'}{\overline{K_m}}d\sigma' d\sigma}. \tag{4b}$$

$$[ESCO]=\overline{Z}\overline{K'_m\frac{\partial u'}{\partial \sigma}}-\int_{\sigma}^{0}\left(\overline{Z'\frac{\partial}{\partial \sigma}\left(K'_m\frac{\partial u'}{\partial \sigma}\right)}+\overline{Z'\frac{\partial}{\partial \sigma}\left(\overline{K_m}\frac{\partial u'}{\partial \sigma}\right)}+\overline{Z'\frac{\partial}{\partial \sigma}\left(K'_m\frac{\partial \overline{u}}{\partial \sigma}\right)}\right)d\sigma, \tag{4c}$$

On the right-hand side of Eq. (4a), the first term is hereafter called the barotropic component of the residual velocity as it results from a barotropic pressure gradient, and the second term is the ESCO component as it results from the ESCO stress, representing a driving force component.

Corresponding to Fig. 5, the six components of estuarine circulation at the cross-section were calculated for the two selected tidal cycles. These components showed similar patterns during the spring (Fig. 6) and neap (Fig. 7) tides except for the ESCO flow. The river-induced flow was the dominant component in the inner regime. The density-driven flow had a lateral sheared structure with landward flow in the middle channel and seaward flows over shoals, which accords with the understanding of estuarine gravitational circulation with strong vertical mixing (Wong, 1994). The magnitude of the density-driven flow was small because of the weak along-estuary salinity gradient in the inner regime. The advection-induced flow, which was related to the clockwise lateral circulation, had a transverse structure that showed landward flows in the right part of the cross-section (facing upstream) and seaward flows in the left. The magnitude of the Coriolis-term (fv)-induced flows was one order smaller than those of other components, and was negligible. The Stokes-return flow was relatively weak because of the approximately standing tidal wave. The ESCO flow was generally two-layered with seaward flow near the surface and landward flow near the bottom during the spring tide, and this pattern was reversed during the neap tide, which showed that reverse internal tidal asymmetry generated a residual flow opposite to that induced by typical internal tidal asymmetry. The sum of the six components (the total residual flow in Figs. 6 and 7) was similar to the residual flow directly obtained by taking the tidal mean of the model output ($\overline{u}$), which indicates that the decomposition method is consistent in itself.

The pattern of ESCO flow is determined by the competition between the barotropic and ESCO components (see Eq. (4a)) which compensate for each other to obey continuity. As the ESCO component involves a vertical integral of the ESCO stress (note the negative sign before the integral), it has a sign opposite that of the ESCO stress, and its magnitude increases from the bottom toward the surface. The opposite tidal asymmetry in vertical eddy viscosity between the spring and neap tides led to ESCO stress being negative during the spring tide (Fig. 8b) and positive during the neap tide (Fig. 8f). As a consequence, the driving force component was seaward (landward) during the spring (neap) tide and the barotropic component tended to balance the driving force component (Fig. 8d, h). The transverse patterns of the two components of the ESCO flow showed that the driving force component determined the upper layer of the ESCO flow while the barotropic component determined the lower layer.

The temporal variation of the strength of ESCO flow measured using the section-averaged absolute value of the ESCO flow velocity in the cross-section is shown in Fig. 9. The density-driven flow is also included for comparison. The ESCO flow was generally larger during spring tides and showed a spring–neap variability that was distorted by large river discharge, such as from days 220–260 (Fig. 9b). In several neap tides with very small tidal ranges, the ESCO flow increased abruptly (see the peaks in Fig. 9b). Compared to the density-driven flow, the ESCO flow was generally several times the magnitude of the density-driven flow, which is consistent with findings that the ESCO flow is more important than the density-driven flow in periodically stratified estuaries (Burchard and Hetland, 2010; Cheng et al., 2013).

The driving force component shows that the strength of the ESCO flow is positively related to that of the ECSO term and is inversely related to the tidal mean vertical eddy viscosity. Both the ESCO stress and tidal mean vertical eddy viscosity had spring–neap variabilities (Fig. 9c and d) with larger magnitudes in the spring tides than during the neap tides. The spring–neap variability of the ESCO flow indicates that the magnitude of the residual flow was generally determined by the ESCO stress, whereas extreme low tidal mean vertical eddy viscosities can cause extremely strong flows. It is notable that the tidal mean vertical eddy viscosity was high during large discharge periods because strong river

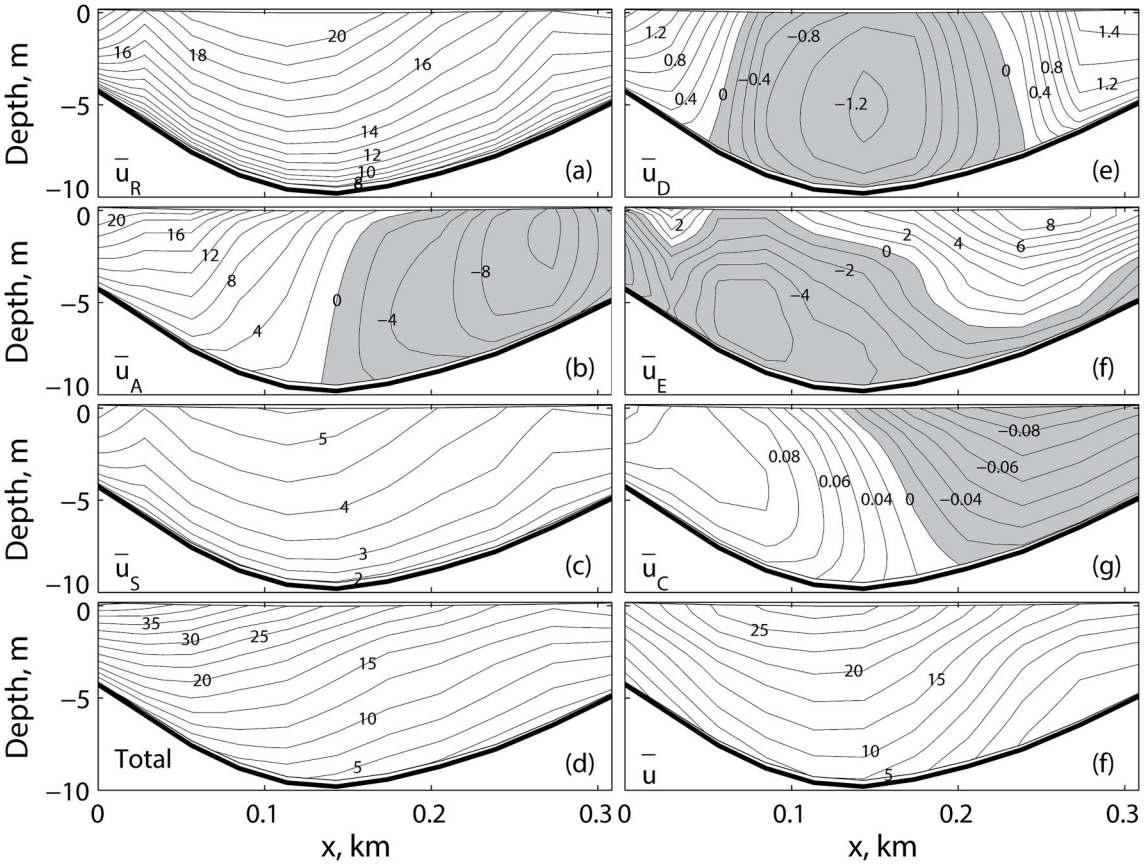

Fig. 6. Cross-channel patterns of river-induced ($\overline{u}_R$), density-driven ($\overline{u}_D$), advection-induced ($\overline{u}_A$), ESCO ($\overline{u}_E$), Stokes return ($\overline{u}_S$), Coriolis-term-induced ($\overline{u}_C$) and total residual flows at the selected cross-channel section during the spring tide (days 80.1–80.6). The first six residual flow components are calculated using the decomposition method, and the total flow is the sum of these six components. $\overline{u}$ is the total residual flow obtained by tidally averaging the modeled current velocity. The residual flows are given in centimeters per second. Negative values (shaded) denote landward flow. The x axis shows the distance from the south bank of the cross-section.

flows pushed the estuary downstream and increased the freshwater-dominant period of a tidal period. The ESCO stress was negative during most of the year because typical internal tidal asymmetry dominated the cross-section. Positive values of the ESCO stress caused by reverse internal tidal asymmetry appeared during neap tides that generally had low tidal ranges and large river discharges, indicating that river flows made important contributions to producing ebb tides with longer durations and stronger currents.

4. Discussion

4.1. ESCO mechanism of barotropic tides

In the shallow water of coastal bays, tidal waves are mostly distorted due to bottom friction and the interaction between the deep channels and shallow water areas, resulting in an asymmetric curve of tidal velocity (or elevation) that has been referred to as tidal asymmetry (Dyer, 1997). The major part of the asymmetry of the tide curve can be represented by superposition of the leading tide and overtide, and the dominance of flood or ebb can be predicted by the phase difference between the overtide and the leading tide (Speer and Aubrey, 1985). The traditional concept of tidal asymmetry focuses on flood dominance or ebb dominance in the tidal current velocity and has not been related to vertical mixing. Because vertical mixing is proportional to the tidal current velocity, tidal velocity asymmetry produces asymmetric tidal mixing between flood and ebb. Dijkstra et al. (2017) identified two types of ESCO circulations: gravitational and tidal ESCO circulations. The latter results from interactions between the barotropic tide and temporal variations of the eddy viscosity. The tidal variation of the vertical eddy viscosity during the freshwater-dominated low-water period in the inner regime has illustrated this process and further indicates that the ESCO flow is also a part of the tidal rectification flow in homogeneous coastal waters. The tidal ESCO flow has a two-layer vertical structure such that it can play an important role in mass transport.

The type of ESCO stress that is generated by tidal velocity asymmetry can be deduced through the ESCO stress ($\overline{K'_m \frac{\partial u'}{\partial z}}$). The tidal residual flow is typically one order of magnitude smaller than the tidal current velocity such that u' is approximately equal to u. In a vertical coordinate that directs positively upward, the sign of $\frac{\partial u'}{\partial z}$ is determined by the direction (or sign) of u because tidal current velocities always increase upward, resulting in a positive vertical gradient. Assuming that the tidal current velocity is positive during the flood tide, if the internal tidal asymmetry is typical, K'_m is positive during the flood tide and negative during the ebb tide, such that $K'_m \frac{\partial u'}{\partial z}$ is positive during both the flood and ebb tides. Thus, the ESCO stress is positive. If internal tidal asymmetry is reversed, K'_m is negative during the flood tide and positive during the ebb tide, such that $K'_m \frac{\partial u'}{\partial z}$ is negative during both the flood and ebb tides. Thus, the ESCO stress is negative. Therefore, the sign of the ESCO stress follows the direction of the current velocity in the tidal phase that has positive K'_m: i.e. flood-dominant tides generate typical tidal asymmetry in vertical eddy viscosity, while ebb-dominant tides generate reverse tidal asymmetry in vertical eddy viscosity.

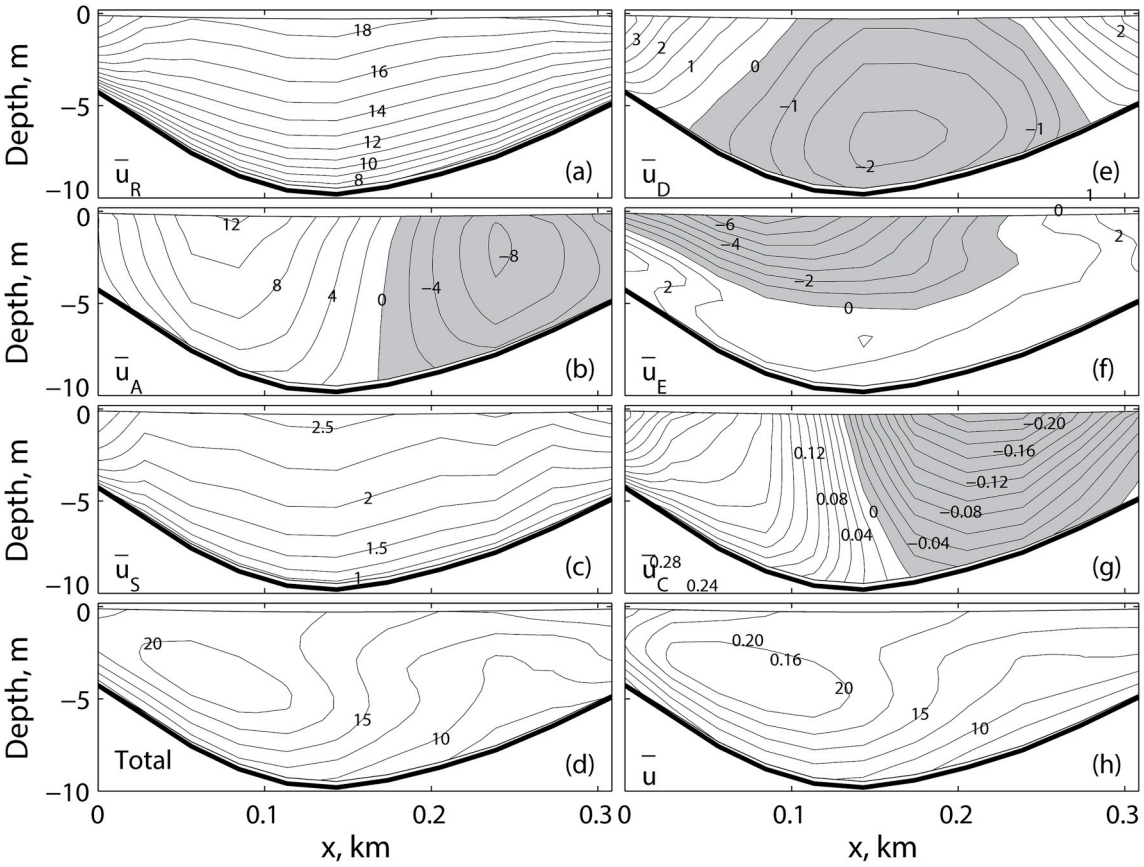

Fig. 7. As Fig. 6, but during the neap tide (day 86.2–86.7).

4.2. Driving mechanisms of the vertical shear of tidal current velocity

As a component of the ESCO stress, the tidal variation of the vertical shear of tidal current velocity determines the sign and magnitude of the ESCO stress. In a one-dimensional conceptual analysis, Jay (1991) showed that tidal variation in vertical mixing (related to stratification) leads to tidal asymmetry in the vertical shear of tidal current velocity, while Burchard and Schuttelaars (2012) found that lateral advection of momentum is the main mechanism that creates the vertical shear of tidal current velocity in estuaries with lateral variability of bottom bathymetry. Because real estuaries mostly have complex bathymetry, examining the driving mechanism of the vertical shear of tidal current velocity helps us to understand the generation of the ESCO flow, which can be achieved through a diagnosis of the vorticity equation in the cross-estuary direction (Becherer et al., 2015):

$$\frac{\partial \omega_y}{\partial t} = \underbrace{-(\boldsymbol{V}\cdot\nabla)\omega_y + (\boldsymbol{\omega}\cdot\nabla)v}_{\text{nonliner terms}} + \underbrace{f\frac{\partial v}{\partial z}}_{\text{Coriolis}} \underbrace{-\frac{\partial}{\partial z}\left[\frac{g}{\rho_0}\frac{\partial}{\partial x}\left(\int_z^{\eta}\rho' dz\right)\right]}_{\text{baroclinicity}} + \underbrace{\frac{\partial^2}{\partial z^2}\left(K_m\omega_y\right)}_{\text{mixing}} \quad (5)$$

where $\boldsymbol{\omega}$ is the vorticity vector, ω_y ($=\frac{\partial u}{\partial z}-\frac{\partial w}{\partial x}$) is the component corresponding to the cross-estuary direction (y), $\boldsymbol{V}$ is the velocity vector, and ρ' ($=\rho-\rho_0$) is the density perturbation. The left-hand side of the equation is the time tendency of the cross-estuary vorticity, and the right-hand side shows the forcing terms: advection of vorticity, vortex stretching/tilting by lateral velocity, tilting of the planetary vorticity f due to the vertical shear in the lateral current, baroclinicity, and vertical mixing. The horizontal diffusion of ω_y is omitted. The first two terms on the right-hand side of the equation are combined and are referred to here as nonlinear terms. According to the definition of ω_y, positive values of the terms in Eq. (5) indicate increasing the vertical shear of the tidal current velocity.

The depth-averaged absolute values of those terms on the right hand side of Eq. (5) in the thalweg of the selected cross-section (the corresponding time series of velocity and salinity are shown in Fig. 5) were compared to evaluate the relative importance of the drivers of ω_y. The analysis concentrated on the high-water period because the changes in vorticity during the freshwater dominant low-water period were less distinct. In the spring tide, advection and mixing were the dominant terms in the vorticity equation, whereas the Coriolis and baroclinicity were negligible (Fig. 10b). The time rate of change of ω_y became important around high water when stratification was strong. Although the magnitudes of advection and mixing were similar, the vertical patterns of the two terms generally had a mirror-image relation, showing that the two processes acted in an opposite way in modifying the vertical shear of the tidal current velocity. During the later flood, advection enhanced the vertical shear (positive values; see Fig. 10c), whereas vertical mixing reduced it (negative values; see Fig. 10d). During the early ebb, advection reduced the vertical shear, whereas vertical mixing enhanced the vertical shear. This was particularly distinct in the upper water column (above −2 m) because the tidal boundary layer in the lower water column was well-mixed (see Fig. 5b).

During the neap tide, advection was the dominant term, and was followed by vertical mixing and the time rate of change in ω_y (Fig. 10f). The patterns of advection and vertical mixing were rather complex, but were still approximate mirror-images (Fig. 10g and h). Due to the relatively stronger stratification, the top layer (above −3 m) was permanently stratified, and the mirror-image relation was mostly distinct in the lower layer. Most of the vertical mixing was negative during the later flood tide reducing the vertical shear of the tidal current velocity, and positive during the early ebb tide increasing the vertical shear. Advection showed an opposite pattern. The diagnosis results for both spring and neap tides confirm that vertical mixing is the main

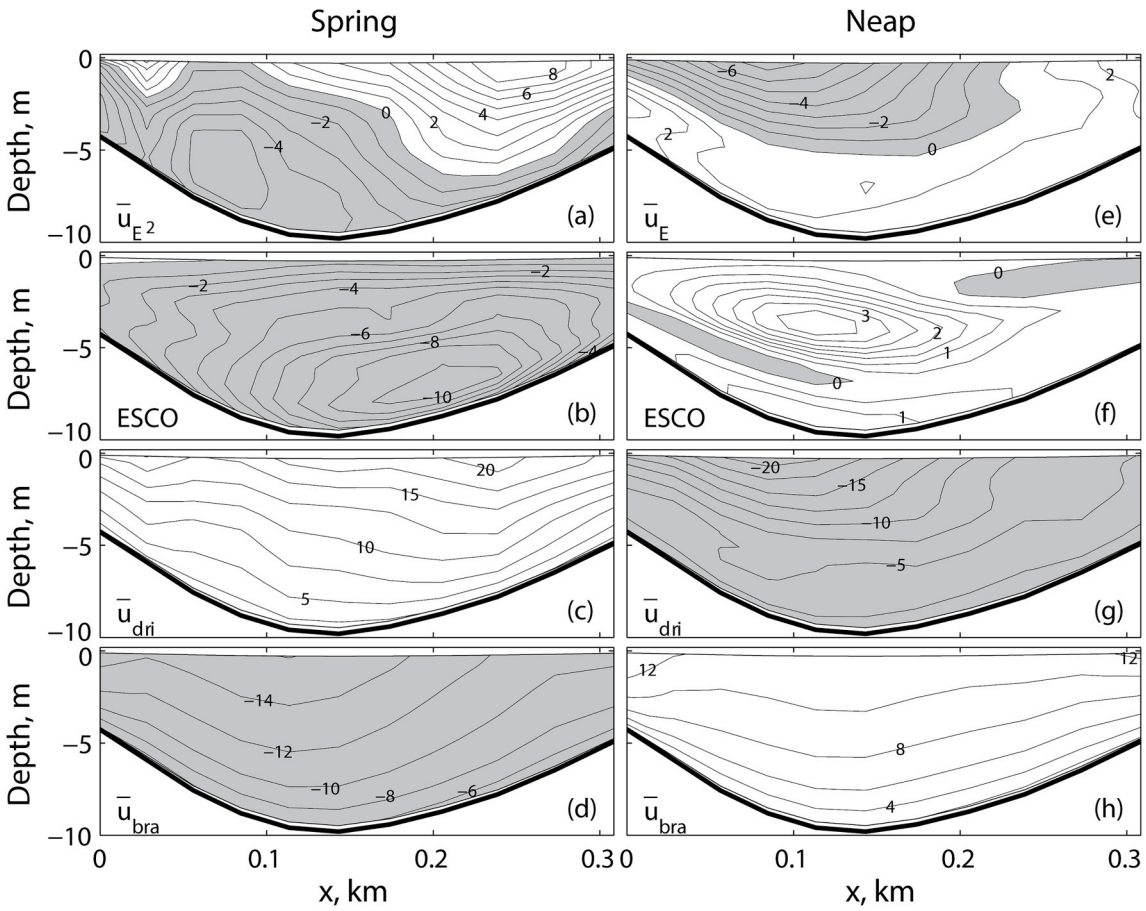

Fig. 8. Cross-channel patterns of ESCO flow ($\overline{u}_E$; first row), ESCO stress (second row), driving force component of ESCO flow ($\overline{u}_{dri}$; third row) and barotropic component of ESCO flow ($\overline{u}_{bra}$; bottom row) at the selected cross-channel section during spring (days 80.1–80.6; left column) and neap (days 86.2–86.7; right column) tides. The residual flows are given in centimeters per second. Negative values (shaded) denote landward flow. The *x* axis shows the distance from the south bank of the cross-section.

driving mechanism that creates the asymmetric vertical shear of tidal current velocity while advection tends to act in an opposite way. Because the selected cross-section is extremely narrow, the roles of vertical mixing and advection in the generation of the vertical shear of tidal current velocity need to be further examined in different types of estuaries.

4.3. Scaling ESCO flow

The strength of ESCO flow has been estimated based on several schemes. As tidal straining is the main mechanism that generates internal tidal asymmetry, Burchard and Hetland (2010) proposed that the magnitude of ESCO flow has a linear relationship with the Simpson number, S_i:

$$S_i = \frac{\frac{g}{\rho_0}\frac{\partial \overline{\rho}}{\partial x}H^2}{C_d U_T^2}, \tag{6}$$

where C_d is the bottom drag coefficient and U_T is the tidal current amplitude. The Simpson number was calculated for each tidal cycle during the entire year in the selected cross-section, and the strength of ESCO flow was measured using the section-averaged absolute values of the ESCO flow velocity (Fig. 11a). The results of the two types of internal tidal asymmetry were plotted separately. The data corresponding to typical internal tidal asymmetry showed a relatively strong linear relationship with a small S_i, but there was no clear relationship for a large S_i. The data corresponding to the reverse internal tidal asymmetry indicated that the strength of the ESCO flow is insensitive to S_i. The above analysis shows that tidal straining is the main driver of the internal tidal asymmetry during the high-wager period, while tidal asymmetries in velocity and duration are the main drivers during the low-water period. The combination of the high-water and low-water periods determines the Internal tidal asymmetry in the inner regime. When tides were strong, S_i was small and the mixing process in the high-water period dominated the tidal cycle. When the tides were weak, S_i was large and the mixing process in the low-water period became important. Therefore, the dependence of ESCO flow strength on S_i became weaker as S_i increased, and became unclear when the reversed internal tidal asymmetry developed.

The analytical study by Cheng et al. (2010) showed that larger asymmetric tidal mixing results in stronger residual flow in periodically stratified estuaries, and a nondimensional parameter K_a was proposed to measure the imbalance of vertical mixing between flood and ebb tides (Cheng et al., 2013). Here, the definition of K_a was slightly modified:

$$K_a = \frac{\frac{1}{T_f}\int_0^{T_f}[K_m]dt - \frac{1}{T_e}\int_0^{T_e}[K_m]dt}{\frac{1}{T_f}\int_0^{T_f}[K_m]dt + \frac{1}{T_e}\int_0^{T_e}[K_m]dt}, \tag{7}$$

where T is the tidal period, T_f and T_e are the durations of the flood and ebb tides, respectively, and the square brackets indicate the depth average. The physical meaning of K_a is the normalized excess vertical mixing over a tidal period. A positive K_a indicates typical asymmetric tidal mixing (more mixing during the flood tide than during the ebb tide), and a negative K_a indicates reverse asymmetric tidal mixing (more mixing in the ebb tide than in the flood tide). The temporal mean eddy

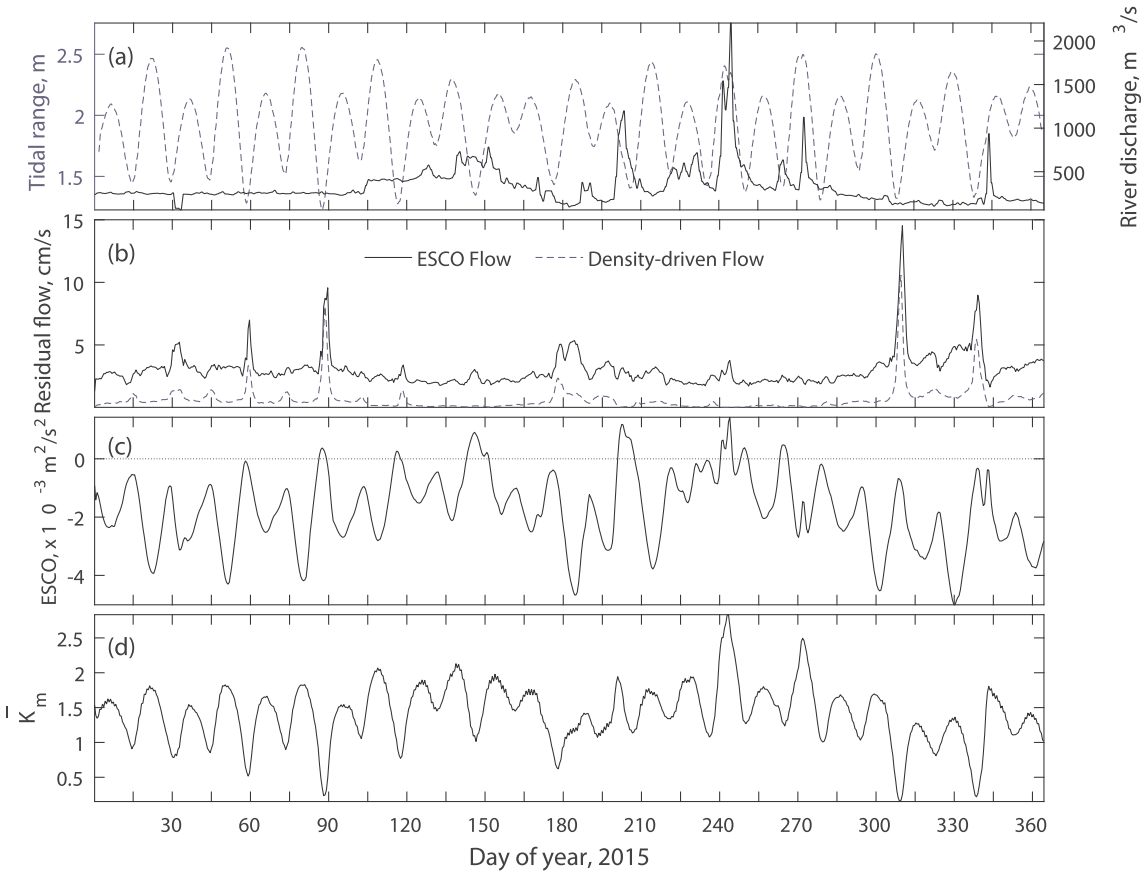

Fig. 9. Daily river discharge of the Jiulong River in 2015 (a). The time series of the tidal range (a), cross-section averaged magnitudes of ESCO and density-driven flows (b), ESCO stress (c) and tidal-mean vertical eddy viscosity at the selected cross-section (d) in 2015.

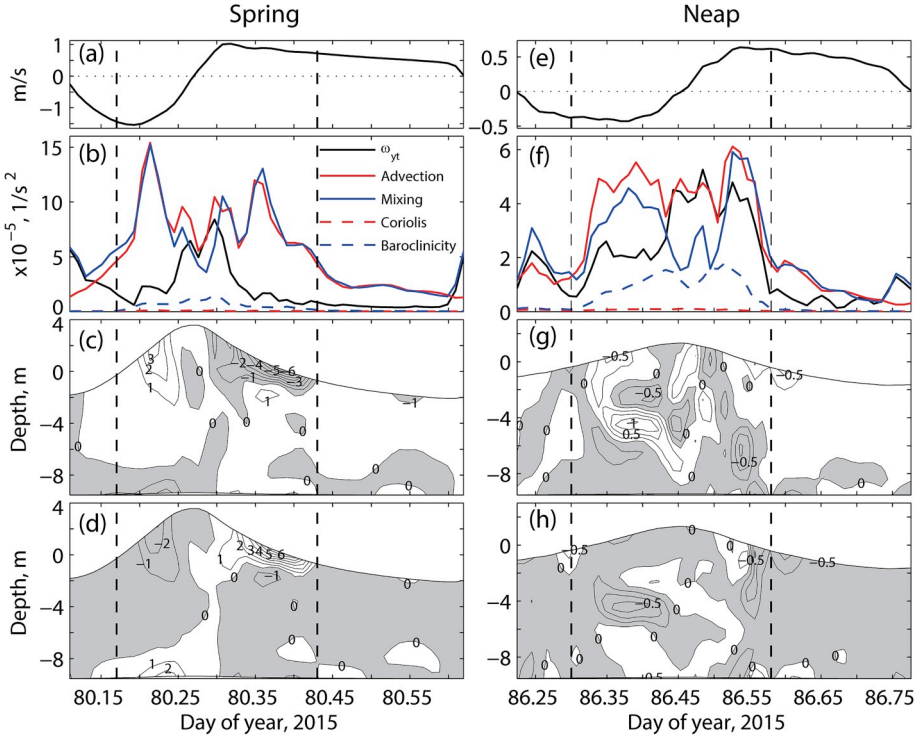

Fig. 10. Diagnosis of the vorticity equation in the cross-estuary direction at the thalweg of the selected cross-channel section in the spring (left column) and neap (right column) tides. The first row shows the depth-mean along-estuary velocity, the second row shows magnitudes of the terms in the vorticity equation, the third row shows vertical profiles of the advection term and the bottom row shows the vertical profiles of the mixing term.

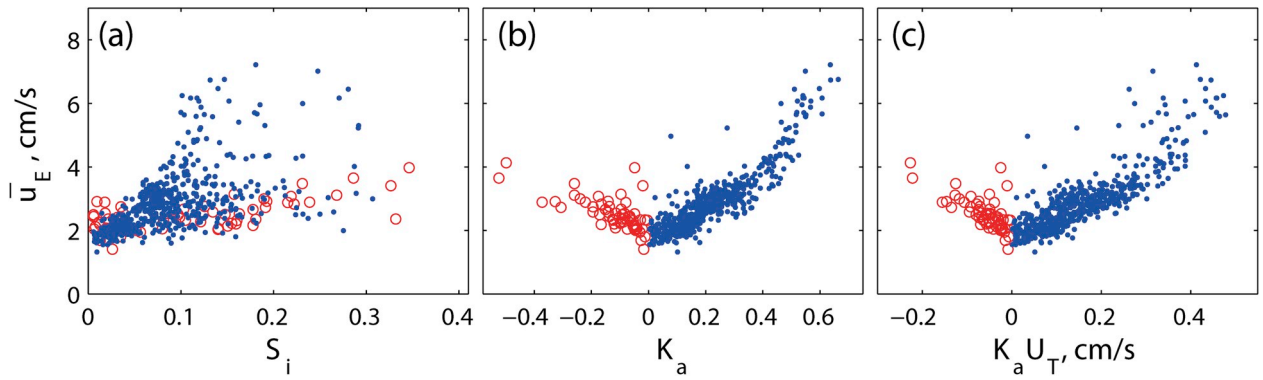

Fig. 11. Magnitude of the ESCO flow at the selected cross-channel section in 2015 as a function of S_i (a), K_a (b), and $K_a U_T$ (c). The blue dots (red circles) show the data during the period with typical (reverse) tidal asymmetry in vertical mixing. (For interpretation of the references to color in this figure legend, the reader is referred to the Web version of this article.)

viscosity was calculated for both the flood and ebb tides to overcome the influence of different flood and ebb tidal durations because the integration of a long duration with weak mixing might be larger than a short duration with strong mixing. The model results showed that the magnitude of the ESCO flow has a linear relationship with K_a for both typical and reverse internal tidal asymmetry when the magnitude of K_a is small (less than 1.0), and it tends to be exponentially related to large K_a (Fig. 11b).

Although K_a is highly related to the strength of the ESCO flow, it is a nondimensional parameter rather than a scale of velocity. According to the solution, the ESCO flow is a function of the asymmetries in tidal mixing (i.e., K_a) and the tidal current amplitude (see the last part of Eq. (4a)):

$$\overline{u_E}\sim\frac{\overline{K'_m h_{bbl}^{U_T}}}{\overline{K_m}} H\sim K_a U_T. \tag{8}$$

Here, we assumed that the thickness of the tidal bottom boundary layer, h_{bbl}, is approximately equal to the mean water depth in the periodically stratified estuary. The results showed a distinct linear relation between the strength of the ESCO flow and $K_a U_T$, although the data points were relatively scattered when $K_a U_T$ was large (Fig. 11c).

4.4. Lateral circulation

The decomposition of estuarine circulation showed that the advection-induced flow has a larger magnitude than those of ESCO and density-driven flows, indicating that lateral circulation could play an important role in estuarine dynamics of the Jiulong River estuary. The selected cross-section was located at a convex bend (toward the northeast; see Fig. 1b), which led to a curvature-driven lateral circulation that was clockwise (facing upstream). The vertical profile of lateral circulation at the thalweg was shown in Fig. 12. The lateral circulation generally had a two-layer structure with northward (positive values) flow near the surface and southward flow near the bottom, consistent with the pattern of a curvature-driven circulation. The clockwise circulation tended to bring saltier water to the south bank, and generated a lateral density gradient, which produced a lateral circulation with opposite pattern as that of the curvature-driven circulation during the slack water (i.e. the high water) because the curvature effect was negligible (Fig. 12a). During the neap tide, the water column was highly stratified during the high-water period, and the relatively complex isohalines produced three-layer flows (Fig. 12b). In the tidal boundary layer (the lower water column), the lateral circulation was two-layer driven by the similar mechanism as that during the spring tide. In the upper layer, the flow resulted from the complex isohalines.

Lateral circulation can make a significant contribution to along-

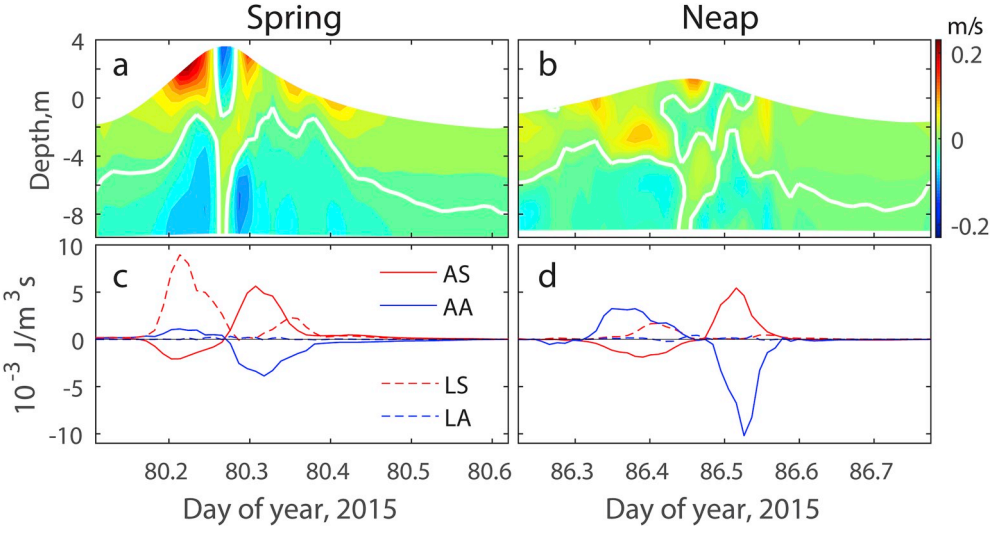

Fig. 12. Tidal variations of the lateral velocity (a, b), and major terms in the potential anomaly equation (c, d) in the thalweg of the selected cross-section during spring (left column) and neap (right column) tides. The white lines in a and b represent 0 m/s. In c and d, AS represents along-estuary straining, AA represents along-estuary advection, LS represents lateral straining, and LA represents lateral advection.

estuary momentum balance. Lerczak and Geyer (2004) proposed that when lateral flows are sufficiently strong to advect water parcels a significant distance over a tidal time scale relative to half the channel breadth (i.e., $4|v|/\omega_T W \geq 1$, where ω_T is the tidal frequency), lateral advection can be expected to play an important role in the longitudinal momentum balance. At the cross-section, the depth-averaged magnitude of lateral circulation was approximately 0.1 m/s, and the resulting $4|v|/\omega_T B$ was about 9.5 (here, the M_2 tidal frequency was used, and $B =$ 0.3 km). The fact that the advection-induced flow obtained by the decomposition method has a larger magnitude than that of ESCO flow (Figs. 6 and 7) further confirmed the importance of lateral circulation in along-estuary momentum balance.

Lateral circulation modifies stratification in estuaries through straining and advection. To evaluate the importance of lateral circulation in estuarine stratification, we applied the potential energy anomaly (ϕ) method that was developed by Simpson et al. (1990) and was further extended by de Boer et al. (2008) and Burchard and Hofmeister (2008):

$$\frac{\partial \phi}{\partial t} = \frac{g}{D}\int_{-H}^{\eta} \tilde{u}\frac{\partial < \rho >}{\partial x}dz + \frac{g}{D}\int_{-H}^{\eta} \tilde{v}\frac{\partial < \rho >}{\partial y}dz + \frac{g}{D}\int_{-H}^{\eta} < u > \frac{\partial \tilde{\rho}}{\partial x}dz + \frac{g}{D}\int_{-H}^{\eta} < v > \frac{\partial \tilde{\rho}}{\partial y}dz + \cdots, \quad (9)$$

with the definition of ϕ being

$$\phi = \frac{1}{D}\int_{-H}^{\eta} gz(\langle \rho > -\rho)dz, \quad (10)$$

where the angle bracket represents the depth-average, for example, $< \rho > = \frac{1}{D}\int_{-H}^{\eta} \rho dz$, $\tilde{u} = u - < u >$, $\tilde{v} = v - < v >$. According to the definition of ϕ, a positive value of ϕ_t indicates increasing stratification. On the right-hand side of Eq. (9), four processes related to along- and cross-estuary circulations were presented and the other terms were omitted. The first term is along-channel straining (also known as tidal straining), the second is lateral straining, the third is along-estuary advection, and the fourth is lateral advection. The four terms in Eq. (9) at the thalweg of the cross-section during the two selected tidal cycles are compared (Fig. 12) to evaluate the relative contributions of the four processes.

The tidal variations of the four terms in Eq. (9) show how the four processes contribute to the mixing/stratification at the cross-section. During the spring tide, along-estuary straining reduced stratification during the flood (negative values) and increased stratification during the ebb (positive values). The along-estuary advection transported stratified water upstream during the flood and transported nearly well-mixed water downstream during the ebb, which affected the stratification in an opposite way than tidal straining did. Lateral straining enhanced stratification over the entire tidal cycle and was weak around the slack water. As lateral straining is the advection of the lateral density gradient by the vertical shear of lateral circulation, this term is related to lateral circulation. The salinity was higher near the north bank than near the south, generating a positive lateral density gradient (note that the cross-channel direction was positive to the right). The lateral circulation brought saltier water from the north bank to the south through the bottom layer and brought fresher water back to the north bank through the top layer, thereby increasing stratification in the cross-section. At the high-water, the direction of both lateral circulation and density gradient were reversed, such that the lateral straining was also positive. The lateral advection was negligible compared to other terms because of the small magnitude of the lateral circulation. During the neap tide, the tidal variations of the four terms in the potential energy anomaly equation showed similar trends to those exhibited in the spring tide but were modified by the stronger stratification. The lateral circulation was suppressed and the lateral straining was smaller. The magnitude of along-estuary advection increased during the flood by bringing relatively more stratified water upstream. The above analysis confirmed that the lateral circulation is not negligible in mixing and dynamics in the Jiulong River estuary.

5. Conclusions

This study investigated the inner regime of the Jiulong River estuary using a three-dimensional numerical model. An important feature of the inner regime was the migration of the saltwater/freshwater interface which leads to a saltwater-dominant high-water period and a freshwater-dominant low-water period. The driving mechanisms of tidal variation in vertical mixing in the two periods differed. During the high-water period, tidal straining was the main driver for reducing stratification during the later flood and enhancing stratification during the early ebb. During the low-water period, internal tidal asymmetry was caused by the flood-ebb asymmetry in the tidal current velocity. The combined mixing processes during the two periods determined the internal tidal asymmetry of a tidal cycle. When the tidal range was large (normal and spring tides), the relatively strong flood tide and tidal straining produced typical internal tidal asymmetry. When the tidal range was small (weak neap tides and relatively large river discharge), the ebb tide had a longer duration and larger current velocities, resulting in a reverse internal tidal asymmetry over the tidal period.

Internal tidal asymmetry generates residual currents through the ESCO stress in the along-estuary momentum equation. The typical internal tidal asymmetry had negative ESCO stress and drove a two-layer residual flow with a landward flow near the bottom and a seaward flow near the surface. The reverse internal tidal asymmetry had negative ESCO stress and drove a two-layer residual flow opposite that generated by the typical tidal asymmetry. The magnitude of the ESCO flow was several times greater than the density-driven flow and exhibited spring-neap tidal variability due to the ESCO stress, which was positively related to tidal range. However, extremely strong ESCO flows occurred during weak neap tides because the strength of the ESCO flow is inversely related to vertical mixing. A simple scale of the ESCO flow was developed and showed that the magnitude of the ESCO flow is linearly related to the tidal current amplitude with a proportion of the asymmetry in tidal mixing, K_a.

A diagnosis of the vorticity equation in the cross-estuary direction was conducted to determine the driving mechanisms of the vertical shear of the tidal current velocity, and the results showed that vertical mixing and lateral advection are the main drivers. Vertical mixing tended to reduce the vertical shear of the tidal current during flood tides and increase the vertical shear during ebb tides, whereas lateral advection tended to compensate for the effect of vertical mixing.

The reverse internal tidal asymmetry revealed in the low-water period has an important implication: the duration and velocity asymmetries of barotropic tides lead to asymmetric mixing between flood and ebb tides. The concepts of internal tidal asymmetry and ESCO flow originally developed in estuaries may be extended to coastal tidal waters that have no stratification. An in-depth analysis of the ESCO flow of barotropic tides would help improve the traditional theories of tidal rectification flow and needs future studies.

Declaration of competing interest

All authors declare that we have no financial and personal relationships with other people or organizations that can inappropriately influence our work, there is no professional or other personal interest of any nature or kind in any product, service and/or company that could be construed as influencing the position presented in, or the review of, the manuscript entitled.

Acknowledgements

P. Cheng thanks the financial support from the National Natural Science Foundation of China (grant no. 41476004) and the National Basic Research Program of China (grant no. 2015CB954004). A. Wang thanks the financial support from the National Natural Science Foundation of China (grant no. 41376070). N. Chen thanks the financial support from the National Natural Science Foundation of China (grant no. 41676098) and Fundamental Research Funds for the Central Universities (20720160120,20720180119). We thank the crew of the R/V Ocean II for their assistance on the cruises. This work was carried out as part of the collaborative program of Physical-Biogeochemical Processes initiated by the State Key Laboratory of Marine Environment Science (MELRI1504). The in situ and numerical model data used in this study are available upon request from P. Cheng (pcheng@xmu.edu.cn). We are grateful to the two anonymous reviewers for their insightful comments, which greatly improved this work.

References

Becherer, J., Burchard, H., Flöser, G., Mohrholz, V., Umlauf, L., 2011. Evidence of tidal straining in well-mixed channel flow from micro-structure observations. Geophys. Res. Lett. 38, 2–6. https://doi.org/10.1029/2011GL049005.

Becherer, J., Stacey, M.T., Umlauf, L., Burchard, H., 2015. Lateral circulation generates flood tide stratification and estuarine exchange flow in a curved tidal inlet. J. Phys. Oceanogr. 45, 638–656. https://doi.org/10.1175/JPO-D-14-0001.1.

Burchard, H., Hetland, R.D., 2010. Quantifying the contributions of tidal straining and gravitational circulation to residual circulation in periodically stratified tidal estuaries. J. Phys. Oceanogr. 40, 1243–1262. https://doi.org/10.1175/2010JPO4270.1.

Burchard, H., Hetland, R.D., Schulz, E., Schuttelaars, H.M., 2011. Drivers of residual estuarine circulation in tidally energetic estuaries: straight and irrotational channels with parabolic cross section. J. Phys. Oceanogr. 41, 548–570. https://doi.org/10.1175/2010JPO4453.1.

Burchard, H., Hofmeister, R., 2008. A dynamics equation for the potential energy anomaly for analyzing mixing and stratification in estuaries and coastal seas. Estuar. Coast Shelf Sci. 77, 679–687. https://doi.org/10.1016/j.ecss.2007.10.025.

Burchard, H., Schuttelaars, H.M., 2012. Analysis of tidal straining as driver for estuarine circulation in well mixed estuaries. J. Phys. Oceanogr. 42, 261–271. https://doi.org/10.1175/JPO-D-11-0110.1.

Chen, W., de Swart, H.E., 2018. Estuarine residual flow induced by eddy viscosity-shear covariance: dependence on axial bottom slope, tidal intensity and constituents. Cont. Shelf Res. 167, 1–13.

Cheng, P., Valle-Levinson, A., de Swart, H.E., 2010. Residual currents induced by asymmetric tidal mixing in weakly stratified narrow estuaries. J. Phys. Oceanogr. 40, 2135–2147. https://doi.org/10.1175/2010JPO4314.1.

Cheng, P., Valle-Levinson, A., de Swart, H.E., 2011. A numerical study of residual circulation induced by asymmetric tidal mixing in tidally dominated estuaries. J. Geophys. Res. 116, C01017. https://doi:10.1029/2010JC006137.

Cheng, P., de Swart, H.E., Valle-Levinson, A., 2013. Role of asymmetric tidal mixing in the subtidal dynamics of narrow estuaries. J. Geophys. Res. Ocean. 118, 2623–2639. https://doi:10.1002/jgrc.20189.

Cheng, P., 2014. Decomposition of residual circulation in estuaries. J. Atmos. Ocean. Technol. 31 (3), 698–713. https://doi.org/10.1175/JTECH-D-13-00099.1.

de Boer, G.J., Pietrzak, J.D., Winterwerp, J.C., 2008. Using the potential energy anomaly equation to investigate tidal straining and advection of stratification in a region of freshwater influence. Ocean Model. 22, 1–11. https://doi.org/10.1016/j.ocemod.2007.12.003.

Dijkstra, Y.M., Schuttelaars, H.M., Burchard, H., 2017. Generation of exchange flows in estuaries by tidal and gravitational eddy viscosity-shear covariance (ESCO). J. Geophys. Res. Ocean. 122, 4217–4237. https://doi:10.1002/2016JC012379.

Dyer, K.R., 1997. Estuaries: A Physical Introduction, second ed. John Wiley, p. 195.

Egbert, G.D., Erofeeva, S.Y., 2002. Efficient inverse modeling of barotropic ocean tides. J. Atmos. Ocean. Technol. 19 (2), 183–204. https://doi.org/10.1175/1520-0426(2002)019<0183:EIMOBO>2.0.CO;2.

Egbert, G.D., Bennett, A., Foreman, M., 1994. TOPEX/Poseidon tides estimated using a global inverse model. J. Geophys. Res. 99 (C12), 24821–24852. https://doi:10.1029/94JC01894.

Fram, J.P., Martin, M., Stacey, M.T., 2007. Exchange between the coastal ocean and a semi-enclosed estuarine basin: dispersive fluxes. J. Phys. Oceanogr. 37, 1645–1660. https://doi:10.1175/JPO3078.1.

Friedrichs, C.T., Aubrey, D.G., 1988. Non-linear tidal distortion in shallow well-mixed estuaries: a synthesis. Estuar. Coast Shelf Sci. 38, 157–172. https://doi.org/10.1016/0272-7714(88)90082-0.

Geyer, W.R., Trowbridge, J.H., Bowen, M.M., 2000. The dynamics of a partially mixed estuary. J. Phys. Oceanogr. 30, 2035–2048. https://doi.org/10.1175/1520-0485(2000)030<2035:TDOAPM>2.0.CO;2.

Guo, W.D., Yang, L.Y., Hong, H.S., Stedmon, C.A., Wang, F.L., Xu, J., Xie, Y., 2011. Assessing the dynamics of chromophoric dissolved organic matter in a subtropical estuary using parallel factor analysis. Mar. Chem. 124, 125–133. https://doi.org/10.1016/j.marchem.2011.01.003.

Haidvogel, D.B., Arango, H., Hedstrom, K., Beckmann, A., Malanotte-Rizzoli, P., Shchepetkin, A., 2000. Model evaluation experiments in the North Atlantic Basin: simulations in nonlinear terrain-following coordinates. Dyn. Atmos. Oceans 32, 239–281. https://doi:10.1016/S0377-0265(00)00049-X.

Hansen, D.V., Rattray, M., 1965. Gravitational circulation in straits and estuaries. J. Mar. Res. 23, 104–122.

Jay, D.A., 1991. Internal asymmetry and an harmonicity in estuarine flows. In: Parker, B. B. (Ed.), Process in Tidal Hydrodynamics. John Wiley, pp. 521–546.

Jay, D.A., Musiak, J.D., 1994. Particle trapping in estuarine tidal flows. J. Geophys. Res. 99, 445–461. https://doi.org/10.1029/94JC00971.

Jiang, Y.W., Wai, O.W.H., 2005. Drying–wetting approach for 3D finite element sigma coordinate model for estuaries with large tidal flats. Adv. Water Resour. 28, 779–792. https://doi:10.1016/j.advwatres.2005.02.004.

Lacy, J.R., Stacey, M.T., Burau, J.R., Monismith, S.G., 2003. The interaction of lateral baroclinic forcing and turbulence in an estuary. J. Geophys. Res. 108 (C3), 3089. https://doi:10.1029/2002JC001392.

Lerczak, J.A., Geyer, W.R., 2004. Modeling the lateral circulation in straight, stratified estuaries. J. Phys. Oceanogr. 34, 1410–1428. https://doi.org/10.1109/RAST.2003.1303919.

Liu, W., Chen, F., Zhou, D., 1994. Formation and evolution of the shoal estuarine channel to Haichang Harbour, Xiamen. J. Oceanogr. Taiwan Strait 13, 317–322 (in Chinese with an English abstract).

Pritchard, D.W., 1956. The dynamic structure of a coastal plain estuary. J. Mar. Res. 15 (1), 33–42.

Pu, X., Shi, J.Z., Hu, G., Xiong, L., 2015. Circulation and mixing along the North passage in the changjiang River estuary, China. J. Mar. Syst. 148, 213–235.

Saha, S., Coauthors, 2014. The NCEP climate forecast system version 2. J. Clim. 27, 2185–2208. https://doi:10.1175/JCLI-D-12-00823.1.

Shchepetkin, A.F., McWilliams, J.C., 2005. The Regional Ocean Modeling System: a split-explicit, free-surface, topography-following coordinates ocean model. Ocean Model. 9, 347–404. https://doi:10.1016/j.ocemod.2004.08.002.

Simpson, J.H., Brown, J., Matthews, J., Allen, G., 1990. Tidal straining, density currents, and stirring in the control of estuarine stratification. Estuaries 13 (2), 125–132. https://doi:10.2307/1351581.

Simpson, J.H., Williams, E., Brasseur, L.H., Brubaker, J.M., 2005. The impact of tidal straining on the cycle of turbulence in a partially stratified estuary. Cont. Shelf Res. 25, 51–64. https://doi.org/10.1016/j.csr.2004.08.003.

Speer, P.E., Aubrey, G.G., 1985. A study of non-linear tidal propagation in shallow inlet/estuarine systems Part II: theory. Estuar. Coast Shelf Sci. 21, 207–224. https://doi.org/10.1016/0272-7714(85)90097-6.

Stacey, M.T., Burau, J.R., Monismith, S.G., 2001. Creation of residual flows in a partially stratified estuary. J. Geophys. Res. 106, 17013–17037. https://doi:10.1029/2000JC000576.

Stacey, M.T., Fram, J.P., Chow, F.K., 2008. Role of tidally periodic density stratification in the creation of estuarine subtidal circulation. J. Geophys. Res. 113, C08016. https://doi:10.1029/2007JC004581.

Wang, Y.P., Voulgaris, G., Li, Y., Yang, Y., Gao, J., Chen, J., Gao, S., 2013. Sediment resuspension, flocculation, and settling in a macrotidal estuary. J. Geophys. Res. Ocean. 118. https://doi:10.1002/jgrc.20340.

Warner, J.C., Geyer, W.R., Lerczak, J.A., 2005. Numerical modeling of an estuary: a comprehensive skill assessment. J. Geophys. Res. 110, C05001. https://doi:10.1029/2004JC002691.

Wong, K.-C., 1994. On the nature of transverse variability in a coastal plain estuary. J. Geophys. Res. 99 (C7), 14 209–14 222. https://doi.org/10.1029/94JC00861.